Astronomy & Astrophysics manuscript no. aa-galevol
September 13, 2010

Galaxy Evolution and Star Formation Efficiency at 0.2 < z < 0.6 ⋆

F. Combes[1], S. García-Burillo[2], J. Braine[3], E. Schinnerer[4], F. Walter[4], and L. Colina[5]

[1] Observatoire de Paris, LERMA (CNRS:UMR8112), 61 Av. de l'Observatoire, F-75014, Paris, France e-mail: francoise.combes@obspm.fr
[2] Observatorio Astronómico Nacional (OAN)-Observatorio de Madrid, Alfonso XII, 3, 28014-Madrid, Spain
[3] Observatoire de Bordeaux, Université Bordeaux I, BP 89, 33270 Floirac, France
[4] Max-Planck-Institut für Astronomie (MPIA), Königstuhl 17, 69117 Heidelberg, Germany
[5] IEM, Consejo Superior de Investigaciones Cientificas (CSIC), Serrano 121, 28006 Madrid, Spain

Received XXX 2010/ Accepted YYY 2010

ABSTRACT

We present the results of a CO line survey of 30 galaxies at moderate redshift (z ∼ 0.2-0.6), with the IRAM 30m telescope, with the goal to follow galaxy evolution and in particular the star formation efficiency (SFE) as defined by the ratio between far-infrared luminosity and molecular gas mass ($L_{FIR}/M(H_2)$). The sources are selected to be ultra-luminous infrared galaxies (ULIRGs), with L_{FIR} larger than 2.8 10^{12} $L_\odot$, experiencing starbursts: their gas consumption time-scale is lower than 10^8 yr. To date only very few CO observations exist in this redshift range that spans nearly 25% of the universe's age. In addition, considerable evolution of the star formation rate is already observed during this period. 18 galaxies out of our sample of 30 are detected (of which 16 are new detections), corresponding to a detection rate of 60%. The average CO luminosity for the 18 galaxies detected is L'_{CO} = 2 10^{10} $L_\odot$, corresponding to an average H_2 mass of 1.6 10^{10} $M_\odot$. The FIR luminosity correlates well with the CO luminosity, in agreement with the correlation found for low and high redshift ULIRGs. Although the conversion factor between CO luminosity and H_2 mass is uncertain, even when taking the lower value assumed for ULIRGs, we find that the maximum amount of gas available for a single galaxy is quickly increasing as a function of redshift. Using the same conversion factor, the SFEs for z∼0.2-0.6 ULIRGs are found to be significantly higher, by a factor 3, than for local ULIRGs, and are comparable to high redshift ones. We compare this evolution to the expected cosmic H_2 abundance and the cosmic star formation history.

Key words. Galaxies: high redshift — Galaxies: ISM — Galaxies: starburst — Radio lines: Galaxies

1. Introduction

Ultra-Luminous Infra-Red Galaxies (ULIRGs) emit most of their energy in the far-infrared, and have far-infrared luminosities $L_{FIR} > 10^{12}$ $L_\odot$, (e.g. Sanders & Mirabel 1996). Since they can be seen so far away, they allow us to explore the evolution of star formation in the universe, and of the star formation efficiency (SFE), in particular defined as the FIR luminosity to H_2 mass ratio (e.g. Kennicutt 1998). Since the discovery of the first high redshift object in CO line emission (IRAS F10214+4724 at z=2.3, Brown & Vanden Bout 1991, Solomon et al. 1992), there has been a wealth of CO-line discoveries, a hundred objects are now detected at z>1, either from ULIRGs, or from LIRGs ($L_{FIR} > 10^{11}$ $L_\odot$). Some are amplified by gravitational lensing (see the review by Solomon & Vanden Bout 2005). They allow us to observe the interstellar medium of the galaxies, the CO excitation (e.g. Weiss et al. 2007) and estimate the amount of molecular gas present. Stars form from molecular gas, so it is important to infer the H_2 mass in order to determine the SFE. At high redshift, many of these objects are quasars or radio-galaxies (due to their selection, e.g. Omont et al. 2003), however, their FIR emission is powered predominantly by star formation (e.g. Riechers et al. 2009, Wang et al. 2010).

Locally, our knowledge of the ULIRGs phenomenon is more profound due to higher spatial resolution and sensitivity. Because the peak of the dust emission is progressively shifted from the FIR to the submm domain, the dust emission can be detected to high redshifts (negative K-correction, e.g. Blain & Longair 1996). The CO-line emission is less favoured, and CO lines are difficult to detect at high z although observing the high-J CO lines helps significantly in highly excited objects (Combes et al. 1999). To date, more than a hundred objects have been studied in detail locally. In the case of the ULIRGs, it was found that they are characterized by compact, nuclear starbursts (e.g. Downes & Solomon 1998), and it has been argued that a special CO-to-H_2 conversion factor should be used, that is 5.75 lower than the standard factor commonly used for Milky Way-like galaxies (Downes et al. 1993). In the present paper, we will adopt for ULIRGs the ratio α=0.8 (Solomon et al. 1997) between $M(H_2)$ and L'_{CO}, expressed in units of $M_\odot$ (K km s^{-1} pc^2)$^{-1}$, and not the standard α=4.6.

At intermediate redshifts, between 0.2 < z < 1, there is a dearth of CO-line detections. This is partly due to observational difficulties. The most commonly used millimetric window is the 3mm one, which is least affected by atmospheric opacity. Between 81 and 115 GHz, all redshifts can be observed with at least one line of the CO rotational ladder, except between z=0.4 and 1. The latter can be observed at 2mm (targeting the CO(2-1) line), but in less favorable atmospheric conditions. While between z=0.2 and z=0.4 the 3mm window can be used in the CO(1-0) transition, the K-correction is strongly reducing

Send offprint requests to: F. Combes
⋆ Based on observations carried out with the IRAM 30m telescope. IRAM is supported by INSU/CNRS (France), MPG (Germany) and IGN (Spain)

its observable intensity (by a factor growing faster than $(1+z)^4$, Combes et al. 1999). The redshift range 0.2 < z < 1 is important though, as it covers almost half of the age of the universe, and also the most dramatic change in star formation activity (e.g. Madau et al. 1998, Hopkins & Beacom 2006). In the universal star formation history, the most striking feature is the impressive drop between z=1 and z=0 by at least an order of magnitude (Blain et al. 1999).

Up to now, very little is known about the molecular gas content of galaxies at moderate redshift. The ULIRG sample of Solomon et al. (1997) contains 37 objects, but only 2 have $z > 0.2$. Negative results were obtained in previous studies, conducted about 10yrs ago (Lo et al. 1999, Wilson & Combes 1998), but the performances of the mm-instruments have dramatically improved since then. Two more objects were detected by Geach et al. (2009), although more upper limits were also reported (Melchior & Combes 2008). To study star forming galaxies in this period, and in particular to derive their star formation efficiency, we have undertaken a CO-line search in the range $0.2 < z < 0.6$, almost unknown territory as far as molecular lines are concerned. We have selected a sample of 30 IR-luminous galaxies in this redshift range to check whether the variation of star forming activity is due to a variation in molecular gas content or star formation efficiency, or both. One of the objects (IRAS 11582+3020, hereafter G4) has already been mapped with the IRAM Plateau de Bure Interferometer (Combes et al. 2006, paper I). The CO map showed spatially resolved emission on 30kpc scales and revealed a velocity gradient. It was concluded in that paper that not all the molecular gas is confined in a nuclear starburst, but that ~50% of it is extended on galactic scales (25-30kpc). In the present paper, we describe the CO survey carried out with the IRAM 30m telescope. The sample is described in Sect. 2 and the observations in Sect. 3. Results are presented in Sect. 4 and discussed in Sect. 5.

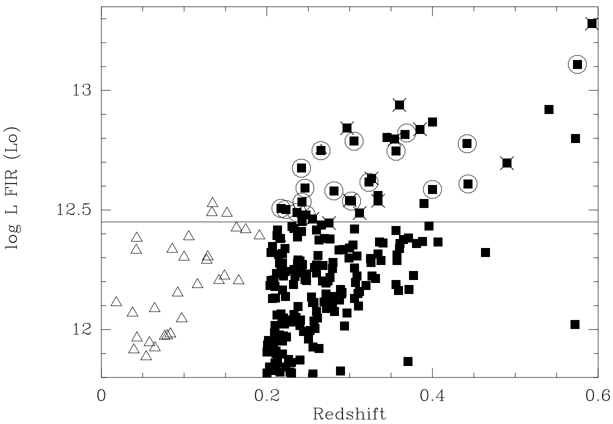

Fig. 1. Definition of our sample. Among the 209 northern galaxies (filled symbols) found in NED between 0.2 < z < 0.6 and detected at 60 μm by IRAS, we selected the most luminous ones (log $L_{\rm FIR}/L_\odot > 12.45$, as indicated by the horizontal line). By comparison, the ULIRGs in the sample of Solomon et al. (1997) are plotted as open triangles. The circles indicate detections, non-detections are marked by a cross. Sources that have neither a circle nor a cross could not be observed due to weather conditions.

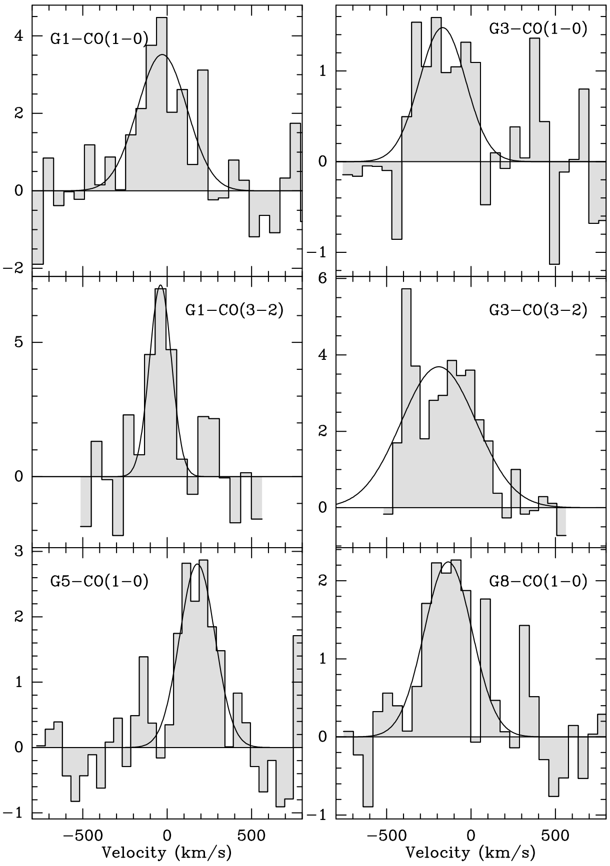

Fig. 2. The CO spectra of the detected galaxies. The zero velocity scale corresponds to the optically determined redshift, listed in Table 1. Sources detected in CO(3–2) at 1mm wavelength are also shown. Some sources were detected in CO(1–0) but not in CO(3–2), as indicated in Table 2. The vertical scale is T_{mb} in mK. The spectrum of G4 is already presented in Paper I.

2. The sample

The present-day sensitivity in the CO line restricted the sample to the brightest objects in the far infrared. We have selected all objects between $0.2 < z < 0.6$ and DEC(2000) > -12° that are identified as galaxies in the literature, have spectroscopic redshifts, and are detected at 60μm (IRAS, ISO). This resulted in a total of 209 galaxies. Most of the galaxies (and in particular the brightest ones) have detailed photometry in the NIR bands, from the samples by Clements et al. (1996), Kim & Sanders (1998), Kim et al. (2002) and Stanford et al. (2000). The available subarcsec K-band images (from either IRTF or Keck telescopes, in the above references), reveal that about two-thirds of the objects are interacting galaxies.

Out of the 209 galaxy sample, we selected the brightest ones, with log $L_{\rm FIR} > 12.45$. This leads to a sample of 36 objects, to be observed with the 30m telescope. We did not reobserve one galaxy detected by Solomon et al. (1997), nor 3C48, detected by Wink et al. (1997), although we include these 2 sources in our analysis. Due to weather conditions, only 28 sources were observed in the project (cf Table 1). Out of the 30 objects in the sample (including the two literature sources), 18 were detected, corresponding to a detection rate of 60%. Figure 1 displays the distribution of FIR luminosities with redshift.

The far-infrared fluxes $F_{\rm FIR}$ are computed as 1.26 x 10^{-14} (2.58 S_{60}+S_{100}) W m^{-2} (Sanders & Mirabel 1996). The far-infrared luminosity is then $L_{\rm FIR} = 4\,\pi\,D_L^2$ CC $F_{\rm FIR}$, where

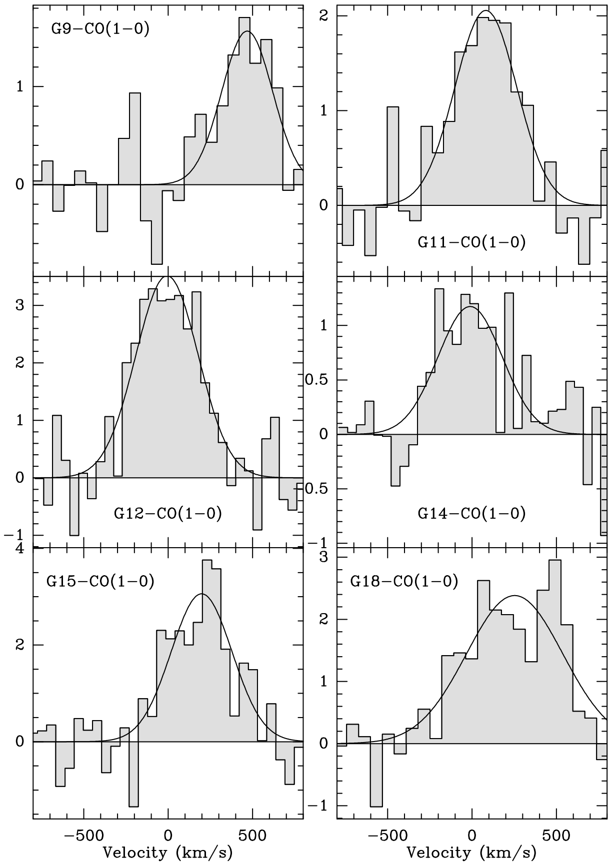

Fig. 3. Same as Fig. 2 for the following galaxies.

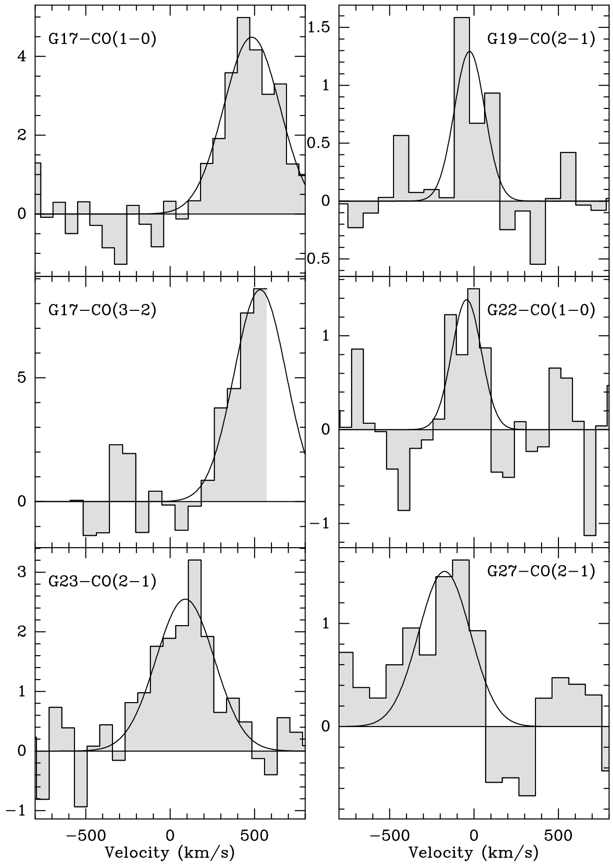

Fig. 4. Same as Fig. 2 for the remaining galaxies.

D_L is the luminosity distance, and CC the color correction, CC=1.42 (e.g. Sanders & Mirabel 1996). The FIR-to-radio ratio q=log([F_{FIR}/(3.75 10^{12} Hz)]/[f_ν(1.4 GHz)]) has been computed for sources where radio data were available (cf Table 2). Excluding the radio galaxies 3C48 and 3C345, the average is q=2.33, typical for ULIRGs (Sanders & Mirabel 1996). The star formation rates of all sample galaxies are above 480 $M_\odot yr^{-1}$, estimated from the infrared luminosity (e.g. Kennicutt 1998).

In this article, we adopt a standard flat cosmological model, with Λ = 0.73, and a Hubble constant of 71 km s^{-1} Mpc^{-1} (Hinshaw et al. 2009).

3. Observations

The observations were carried out with the IRAM 30m telescope at Pico Veleta, Spain, between January 2005 and January 2006. Most of the galaxies, with redshifts between 0.2 and 0.39, could be observed simultaneously at 3mm in CO(1-0) and at 1mm in CO(3-2), except the two lowest redshift sources (G4 and G5) where only observations in the 3mm band were possible. In any case, the weather prevented us sometimes from taking useful data at 1mm. For the highest redshift sources (G19, G20, G23, G27 and G28), only the CO(2-1) line was observed in the 2mm band.

The SIS receivers were tuned in single sideband mode to the redshifted frequencies of the various CO lines. The observations were carried out in wobbler switching mode, with reference positions offset by 3′ in azimuth. We used the 1 MHz back-ends with an effective total bandwidth of 512 MHz at 3 mm (providing a ∼ 1500 km s^{-1} range) and the 4 MHz filterbanks with an effective total bandwidth of 1024 MHz at 1 mm.

We spent 2–4 hours on each galaxy, resulting in a relatively homogeneous noise level of 1–2 mK per 30 km s^{-1} channel for all sources. The system temperatures ranged between 120 and 250 K at 3 mm, between 220 and 300 K at 2 mm, and between 300 and 500 K at 1.2 mm, in T_A^*. The pointing was regularly checked on continuum sources and yielded an accuracy of 3′′ rms. The temperature scale used is in main beam temperature $T_{\rm mb}$. At 3mm, 2mm and 1mm, the telescope half-power beam width is 27′′, 17′′ and 10′′ respectively. The main-beam efficiencies are $\eta_{\rm mb}$ = $T_{\rm A}^*/T_{\rm mb}$=0.85, 0.70 and 0.64, respectively, and $S/T_{\rm mb}$ = 4.8 Jy/K for all bands.

Each spectrum was summed and reduced using linear baselines, and then binned to 50 – 60 km s^{-1} channels for the plots.

4. Results

4.1. CO detection in z=0.2-0.6 ULIRGs

All spectra for CO detections are displayed in Figures 2, 3 and 4 (except G4 reported in paper I). The non-detections are reported in Table 2. Integrated upper limits are computed at 3σ, assuming a common line-width of 300 km s^{-1}, and getting the rms of the signal over 300 km s^{-1}. Lines are assumed detected when the integrated signal is larger than 3σ. Gaussian fits then yielded the central velocities, velocity FWHMs and integrated fluxes listed in Table 2.

As already noticed in Sect. 2, very few objects were previously detected in CO in this redshift range. We include in our analysis, and in Table 2, two additional ULIRGs (G29 and G30) that satisfy our sample criteria. In the discussion, we also added the two galaxies on the outskirts of the cluster Cl 0024+16 (Geach et al. 2009); they are not ULIRGs, but it is interesting to

Table 2. Observed line parameters

Galaxy	Line	$\nu_{\rm obs}$ [GHz]	S(CO)[a] [Jy km s^{-1}]	V^b [km s^{-1}]	$\Delta V_{\rm FWHM}$ [km s^{-1}]	L'$_{\rm CO}$/10^{10} [K km s^{-1} pc^2]	S$_{60}$ [Jy]	S$^c_{100}$ [Jy]	log L$_{\rm FIR}$ [L$_\odot$]	F(1.4GHz)[d] [mJy]
G1	CO(1–0)	88.534	7.5 ± 1.4	-29. ± 33.	398. ± 98.	3.58	0.68	0.77	12.54	
G1	CO(3–2)	265.588	6.2 ± 2.0	-38. ± 21.	148. ± 62.	0.33	0.68	0.77	12.54	
G2	CO(1–0)	83.228	< 1.2			< 0.9	0.67	1.13	12.84	
G2	CO(3–2)	249.672	< 3.2			< 0.3	0.67	1.13	12.84	
G3	CO(1–0)	92.513	2.3 ± 0.5	-168. ± 41.	314. ± 66.	0.73	1.18	1.55	12.59	2.16
G3	CO(3–2)	277.525	9.6 ± 0.9	-185. ± 37.	498. ± 47.	0.33	1.18	1.55	12.59	2.16
G4	CO(1–0)	94.253	6.5 ± 0.7	248. ± 24.	434. ± 52.	1.67	1.23	1.52	12.50	3.09
G5	CO(1–0)	94.718	3.4 ± 0.6	178. ± 20.	240. ± 44.	0.83	1.36	1.54	12.51	25.5
G6	CO(1–0)	90.409	< 1.7			< 0.7	0.72	0.69	12.44	3.0
G7	CO(1–0)	84.758	< 1.7			< 1.2	1.18	1.20	12.94	
G7	CO(3–2)	254.262	< 4.5			< 0.3	1.18	1.20	12.94	
G8	CO(1–0)	93.186	3.4 ± 0.7	-135. ± 32.	301. ± 82.	1.0	0.99	1.43	12.49	5.96
G9	CO(1–0)	92.439	2.1 ± 0.5	469. ± 30.	290. ± 72.	0.67	0.94	1.10	12.48	3.85
G10	CO(1–0)	91.850	< 1.7			< 0.6	0.82	1.04	12.46	7.44
G11	CO(1–0)	89.985	4.5 ± 0.6	85. ± 30.	428. ± 66.	1.86	0.84	1.15	12.58	2.77
G12	CO(1–0)	92.811	7.7 ± 0.8	-5. ± 21.	430. ± 44.	2.33	1.48	1.99	12.68	5.67
G13	CO(1–0)	88.875	< 1.7			< 0.8	1.24	2.13	12.84	
G14	CO(1–0)	92.811	2.4 ± 0.7	-10. ± 70.	420. ± 140.	0.73	1.06	1.43	12.53	
G15	CO(1–0)	88.330	6.9 ± 1.1	200. ± 34.	433. ± 73.	3.38	1.22	1.27	12.79	
G16	CO(1–0)	86.932	< 1.2			< 0.7	0.58	1.14	12.63	40.3
G17	CO(1–0)	82.337	8.3 ± 0.9	478. ± 19.	363. ± 46.	7.14	0.32	0.64	12.59	
G17	CO(3–2)	246.997	12.9 ± 2.0	500. ± 22.	303. ± 56.	1.24	0.32	0.64	12.59	
G18	CO(1–0)	85.008	7.6 ± 0.7	253. ± 32.	651. ± 64.	5.18	0.61	1.22	12.75	2.3
G18	CO(3–2)	255.012	< 4.5			< 0.3	0.61	1.22	12.75	2.3
G19	CO(2–1)	159.874	1.5 ± 0.4	-28. ± 30.	225. ± 63.	0.40	0.53	<0.44	12.78	6.87
G20	CO(2–1)	154.723	< 1.4			< 0.5	0.23	0.57	12.70	8.82
G21	CO(1–0)	88.670	< 1.7			< 0.8	0.71	0.76	12.54	7.78
G21	CO(3–2)	265.997	< 4.5			< 0.2	0.71	0.76	12.54	7.78
G22	CO(1–0)	87.129	1.5 ± 0.3	-41. ± 26.	196. ± 44.	0.82	0.62	0.99	12.62	1.59
G22	CO(3–2)	261.373	< 2.3			< 0.1	0.62	0.99	12.62	1.59
G23	CO(2–1)	159.763	4.7 ± 0.7	91. ± 25.	370. ± 60.	1.27	0.23	0.62	12.61	1.76
G24	CO(1–0)	85.134	< 0.8			< 0.6	0.52	1.83	12.80	
G24	CO(3–2)	255.388	< 4.5			< 0.3	0.52	1.83	12.80	
G25	CO(1–0)	87.859	< 1.2			< 0.6	0.40	1.06	12.49	
G25	CO(3–2)	263.564	< 9.0			< 0.5	0.40	1.06	12.49	
G26	CO(1–0)	86.410	< 1.2			< 0.7	0.46	0.83	12.54	1.36
G26	CO(3–2)	259.217	< 4.5			< 0.3	0.46	0.83	12.54	1.36
G27	CO(2–1)	146.373	2.1 ± 0.6	-126. ± 34.	231. ± 90.	0.95	0.43	<0.94	13.11	2.7
G28	CO(2–1)	144.719	< 1.9			< 0.9	0.60	1.26	13.28	7000
G29[e]	CO(1–0)	84.170	1.9 ± 0.3	-6. ± 10.	270. ± 20.	1.42	0.74	0.83	12.78	16000
G30[f]	CO(1–0)	91.123	3.8 ± 0.4	185. ± 20.	270. ± 30.	1.40	1.45	1.82	12.75	5.49

Quoted errors are statistical errors from Gaussian fits. The systematic calibration uncertainty is 10%.
[a] The upper limits are at 3σ with an assumed ΔV = 300 km s^{-1}. [b] The velocity is relative to the optical redshift given in Table 1.
[c] The 60 and 100μm fluxes are from NED (http://nedwww.ipac.caltech.edu/)
[d] From the FIRST catalog (http://sundog.stsci.edu/). Errors are typically 0.14 mJy
[e] From Wink et al. (1997). [f] From Solomon et al. (1997).

compare star formation efficiencies for all CO-detected objects in this redshift range.

The detection rate of 60% in our sample, down to a sensitivity limit of ∼ 1.5 Jy km s^{-1}, must be considered a lower limit. Indeed, the available velocity range of the receivers (about 1500 km s^{-1}) could have missed some sources, if the optical redshift was not accurate enough. Some galaxies show a significant velocity offset (e.g. G17), as can be seen in Table 2 and the Figures. Some of the profiles may have a double-horn shape as G18, but most do not, given our spectral resolution and sensitivity. The line-widths detected are compatible with massive galaxies at random inclinations. Their average is $\Delta V_{\rm FWHM}$ = 348 km s^{-1}, very similar to the value for local ULIRGs of 302 km s^{-1} (Solomon et al. 1997). In comparison, the submillimeter galaxies have much broader widths, 655 km s^{-1} on average (Greve 2005). Given the angular distance of the sources (average value 1000 Mpc), our beam subtends between 50 and 100kpc, and all galaxies can be considered unresolved, at least as far as their molecular component is concerned.

4.2. CO luminosity and H_2 mass

To derive the total H_2 mass, we first compute the CO luminosity through integrating the CO intensity over the velocity profile.

The CO luminosity for a high-z source is given by

$$L'_{CO} = 23.5 I_{CO} \Omega_B \frac{D_L^2}{(1+z)^3} \ \ \mathrm{K\ km\ s^{-1}\ pc^2}$$

Table 1. Definition of the sample

G	Source	RA(2000)	DEC(2000)	z
G1	IRAS 00302+3625	00:32:57.6	+36:41:56	0.3023
G2	IRAS 08081+2611	08:11:14.4	+26:02:17	0.3850
G3	IRAS 10091+4704	10:12:16.7	+46:49:43	0.2460
G4	IRAS 11582+3020	12:00:46.8	+30:04:15	0.2230
G5	[a]J12054771+1651085	12:05:47.7	+16:51:08	0.2170
G6	[b]J1307006+233805	13:07:00.6	+23:38:05	0.2750
G7	[a]J13301520+3346293	13:30:15.2	+33:46:29	0.3600
G8	IRAS 13352+6402	13:36:50.7	+63:47:03	0.2366
G9	IRAS 13379+3339	13:40:14.4	+33:24:45	0.2473
G10	IRAS 13447+2833	13:47:05.5	+28:18:05	0.2551
G11	IRAS 15298+6319	15:30:41.1	+63:09:40	0.2810
G12	IRAS 16300+1558	16:32:21.4	+15:51:45	0.2417
G13	[HB89] 1821+643	18:21:57.3	+64:20:36	0.2970
G14	IRAS 20551+2441	20:57:19.7	+24:53:37	0.2425
G15	IRAS 23113+0314	23:13:54.3	+03:30:58	0.3053
G16	IRAS 01506+2554	01:53:28.3	+26:09:40	0.3264
G17	IRAS F02115+0226	02:14:10.3	+02:40:00	0.4000
G18	IRAS 07449+3350	07:48:10.6	+33:43:27	0.3560
G19	[b]J0913454+405628	09:13:45.4	+40:56:28	0.4420
G20	IRAS F10156+3705	10:18:34.5	+36:49:52	0.4900
G21	IRAS 12514+1027	12:54:00.8	+10:11:12	0.3000
G22	[HB89] 1402+436	14:04:38.8	+43:27:07	0.3233
G23	[c]J145658.42+333710.1	14:56:58.4	+33:37:10	0.4430
G24	IRAS 19104+8436	19:01:44.5	+84:41:25	0.3544
G25	IRAS F00415-0737	00:44:05.6	-07:21:13	0.3120
G26	[c]J020412.43-005351.4	02:04:12.4	-00:53:51	0.3343
G27	IRAS F00235+1024	00:26:06.5	+10:41:32	0.5750
G28	3C345	16:42:58.8	+39:48:37	0.5928
G29	3C48	01:37:41.3	+33:09:35	0.3695
G30	[c]J140931.25+051131.2	14:09:31.2	+05:11:31	0.2644

[a] 2MASX source; [b] 2MASSi source; [c] SDSS source

where I_{CO} is the intensity in K km s^{-1}, Ω_B is the area of the main beam in square arcseconds and D_L is the luminosity distance in Mpc. We then compute H_2 masses using $M_{H_2} = \alpha$ L'$_{CO}$, with $\alpha = 0.8$ M$_\odot$ (K km s^{-1} pc^2)$^{-1}$, for ULIRGs. The molecular gas masses are listed in Table 4. Although it could be advocated that a different conversion factor should apply to some of the galaxies, we always refer to the M(H_2) mass, directly proportional to CO luminosity, for the sake of comparison. For those galaxies where we observed two CO transitions, we used the CO luminosity of the lower transition to calculate H_2 masses. In our sample, most galaxies have CO(1-0) data, except three galaxies, G19, G23 and G27, which have been detected in CO(2-1). We assume that the brightness temperatures are similar in the two lines, as expected for an optically thick, and thermally excited medium. The problem is more severe for high-z objects, where the CO excitation is not well-known. The average CO luminosity for the 18 galaxies detected is L'$_{CO}$ = 2. 10^{10} L$_\odot$, corresponding to an average H_2 mass of 1.6 10^{10} M$_\odot$.

The star formation efficiency (SFE), also listed in Table 4, is defined as L$_{FIR}$/M(H_2) in L$_\odot$/M$_\odot$. Since the SFR is related to the FIR luminosity as SFR= L$_{FIR}$ /(5.8 10^9L$_\odot$) (e.g. Kennicutt 1998), the gas consumption time-scale can be derived by τ = 5.8/SFE Gyr.

4.3. Molecular gas excitation

Three sources have been detected in both the CO(1-0) and CO(3-2) lines, and three have upper limits (see Table 3). For the data points, we took the peak flux S_ν of the lines, since the CO(3-2) and CO(1-0) have sometimes different measured linewidths, which could be due partly to the noise. The corresponding ratio between the peak brightness temperatures are also displayed in Table 3, to compare more easily with the predictions of the model.

Table 3. CO gas excitation

G	S_{32}/S_{10} [peak]	T_{mb32}/T_{mb10} [peak]	n(H_2) [cm^{-3}] 45K	n(H_2) [cm^{-3}] 20K
G1	2.2 ± 1.1	0.25 ± 0.1	63.	200.
G3	2.6 ± 0.8	0.29 ± 0.09	79.	250.
G17	1.9 ± 0.5	0.21 ± 0.05	46.	140.
G18	< 1.3	< 0.14	<20.	<63.
G22	< 1.0	< 0.11	<12.	<40.

n(H_2), for T_k=45K and 20K, and $N_{CO}/\Delta V = 7\times10^{16}$ cm^{-2}/(km s^{-1})

The peak flux ratio between the two lines S_{32}/S_{10}, and equivalently the peak brightness temperature ratio, is a good indicator of the average density of the emitting medium, since density is the main factor determining the excitation. Another factor is the kinetic temperature, which could be linked to the dust temperature (e.g. Weiss et al 2003). In Table 4, we have computed the dust temperature deduced from the far-infrared fluxes, assuming $\kappa_\nu \propto \nu^\beta$, where κ_ν is the mass opacity of the dust at frequency ν, and $\beta = 1.5$. The average dust temperature for our sample is 46 ± 5 K. This is comparable to recent results for starburst galaxies, which have dust temperatures ≈ 40 K (e.g. Sanders & Mirabel 1996).

If the gas is heated by collisions with the dust, at low density the gas temperature is expected to be lower than the dust temperature. Alternatively, if the gas is heated directly from UV photons near star forming regions, or by shocks due to turbulence or perturbed dynamics, then the gas could be at much higher kinetic temperatures. Since we observe very low excitation temperatures, we consider it unlikely that, in average over the beam, the hot molecular gas is dominating the emission.

Using the Radex code (van der Tak et al. 2007), we have computed the predicted main beam temperature ratio between the CO(3-2) and CO(1-0) lines, for several kinetic temperatures, and as a function of H_2 densities, and CO column densities. Figure 5 shows these predictions for T_k=45 and 20K. The black contours delineated the range of observed values. In Table 3 we list the derived values for the n(H_2) densities, for two values of the kinetic temperatures (45 and 20K), and for a fixed column density per velocity width.

We adopted a column density of N(CO)/ΔV of 7×10^{16} cm^{-2}/(km s^{-1}), which assumes that all CO lines are optically thick. This number is at the right order of magnitude, given the high molecular gas masses derived in Table 2. For M(H_2) = 3 10^{10} M$_\odot$, a typical CO abundance of CO/H_2 = 10^{-4}, and a linewidth of 300 km s^{-1}, this column density will correspond to an homogenous disk of 3 kpc in size. Either the emitting CO gas is more concentrated, as in nuclear starbursts, i.e. the CO column density would be higher, or the gas extent is larger than 3kpc, in which case we would have to take the clumping factor into acount. In any case, it is likely that the CO lines are optically thick.

The excitation of the CO gas appears quite low, implying a low average H_2 density in our galaxies. Comparing to the different excitation patterns observed in other high-z starburst galaxies (Weiss et al. 2007), our galaxies are among the lowest excitation, comparable to the Milky Way or even lower.

It should be kept in mind that error bars are large on the observed ratios. The average ratio is lower than 1.8±0.6, taking into account the upper limits. However the conclusion of a rather low average H_2 density is rather robust with respect to the error bars, since the predicted flux ratio is increasing very quickly with density in the model. We note that even with the extreme hypothesis of optically thin gas, the observations are only compatible with $n(H_2) < 3\,10^3$ cm^{-3}, since the predicted ratio increases even more with density than in the thick case. It is also possible that the gas kinetic temperature is much higher than the dust temperature, but then the derived H_2 density is even lower.

4.4. Variation with redshift

Does the molecular gas content of galaxies evolve with redshift? It is interesting to compare the CO luminosity of our sample with the wealth of data reported in the literature. Figure 6 shows all CO measurements as a function of redshift. This figure reveals that indeed our sample (full black circles) is filling in the CO redshift desert, although not completely. The rise of the CO luminosity that is observed at high redshift (z >1) in fact begins as soon as z=0.2-0.3.

This variation is meaningful in the sense that only the brightest objects have been selected here. Most of the variation with z comes from the fact that there is no extremely luminous objects at z< 0.2. In itself, it is already an interesting evolution, that has been discussed in previous works at high redshift (i.e. Solomon & vanden Bout 2005, Tacconi et al 2010). The present work extends this variation in the intermediate redshift range, and suggests that the increase in gas content with z might begin as soon as z=0.3. The possibility of undiscovered large CO luminosity objects locally is not high, given the good correlation between CO and FIR luminosity. These objects should have been discovered as ULIRGs.

To interpret this evolution, caveats have to be kept in mind. At high redshift, at least for some of the sources, the CO luminosity could be over-estimated by poorly known amplification factors due to lensing. The luminosities have been corrected for amplification, when known, but these uncertainties contribute to the large scatter. This is not the case for the sample from Daddi et al (2010, green circles) or the sample from Genzel et al (2010, blue asterisks). Another uncertainty comes from the CO gas excitation. The CO luminosities of high redshift ULIRGs come from the measured high-J lines, and the low-J lines are often not known. They could underestimate the H_2 mass, since the subthermal excitation is likely to reduce their luminosity with respect to the local objects, observed in CO(1-0). We think, however, that the steep rise at $0.2 < z < 0.6$ of the most luminous galaxies discussed in this paper does not suffer from these caveats (they are detected in majority in CO(1-0) and are not lensed). It is interesting to note that the trend seen in Fig 6 is essentially dominated by three galaxies, G1, G15 and G18, which are particularly strong in CO-emission. No such extreme L'_{CO} has been found in the local universe. Two of these galaxies (G1 and G18) have been shown in Sect. 4.3 to be subthermally excited, and are likely extended starburst with relatively low efficiency, as presented by Daddi et al. (2008). In paper I, we also derived an extended gas disk for G4 with the Plateau de Bure observations. Table 4 confirms that G1 and G18 have among the lowest SFE of the sample. It is conceivable that the conversion factor between L'_{CO} and $M(H_2)$ would be higher in these sources, leading to higher gas mass.

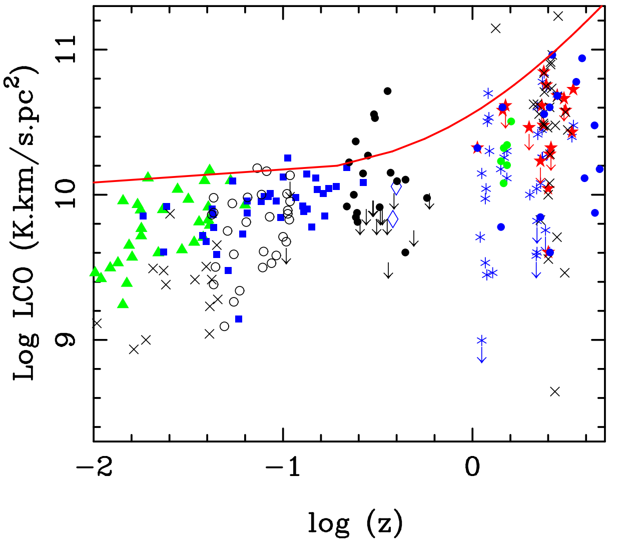

Fig. 6. Measured CO luminosities, corrected from amplification when known, but not for gas excitation, as a function of redshift. We compare our points (full black circles, and arrows as upper limits) with a compilation of high-z molecular gas surveys, and local ones: green triangles are from Gao & Solomon (2004), blue squares from Solomon et al. (1997), open circles from Chung et al. (2009), blue diamonds from Geach et al. (2009), black crosses from Iono et al. (2009), red stars, from Greve et al. (2005), green full circles from Daddi et al. (2010), blue asterisks from Genzel et al. (2010), and blue full circles from Solomon & vanden Bout (2005). The red curve is the power law for Ω_{H_2}/Ω_{HI} proposed by Obreschkow & Rawlings (2009).

4.5. Correlation between FIR and CO luminosities

Figure 7 shows the well studied correlation between FIR and CO luminosities (e.g. Young & Scoville 1991). The correlation is non-linear, with the ultra-luminous objects displaying a higher FIR luminosity (i.e. star formation) for the amount of gas present, as implied by the lines plotted in the Figure. Our sample galaxies fit perfectly in this picture, being all above the curve $L_{FIR}/M(H_2)$=100 $L_\odot/M_\odot$ (corresponding to a consumption timescale of τ =58 Myr). One of the two galaxies detected above $L_{FIR}/M(H_2)$=1000 $L_\odot/M_\odot$ (G19) has indications of nuclear activity (see Type in Table 4) , but the second (G27) has none. We note that they are two of the three galaxies detected in CO(2-1), and not in CO(1-0); we have derived their H_2 masses with the assumption of equal CO luminosity between these two first lines. If their gas was sub-thermally excited, their H_2 mass could then be slightly under-estimated.

Assuming a dust temperature T_d and the observed 100 μm flux S_{100}, we can derive the dust mass as

$$\begin{aligned} M_d &= 4.8 \times 10^{-11} \frac{S_{\nu o}\, D^2_{\rm Mpc}}{(1+z)\kappa_{\nu r}\, B_{\nu r}(T_d)}\ M_\odot \\ &= 5(1+z)^{-(4+\beta)}\, S_{100\mu}\, D^2_{\rm Mpc}\ \{\exp(144(1+z)/T_d) - 1\}\ M_\odot \end{aligned}$$

where $S_{\nu o}$ is the observed FIR flux measured in Jy, $D^2_{\rm Mpc}$ is the luminosity distance in Mpc, $B_{\nu r}$ is the Planck function at the rest frequency $\nu r = \nu o(1+z)$, and we use a mass opacity coefficient of 25 cm^2 g^{-1} at rest-frame 100 μm, (Hildebrand 1983), with a frequency dependence in β=1.5. Estimated dust masses are displayed in Table 4. If we adopt the low conversion factor of α = 0.8 $M_\odot$ (K km s^{-1} pc^2)$^{-1}$, the average gas-to-dust mass ratio is 96 for all the detected galaxies. The gas to dust mass ratio could

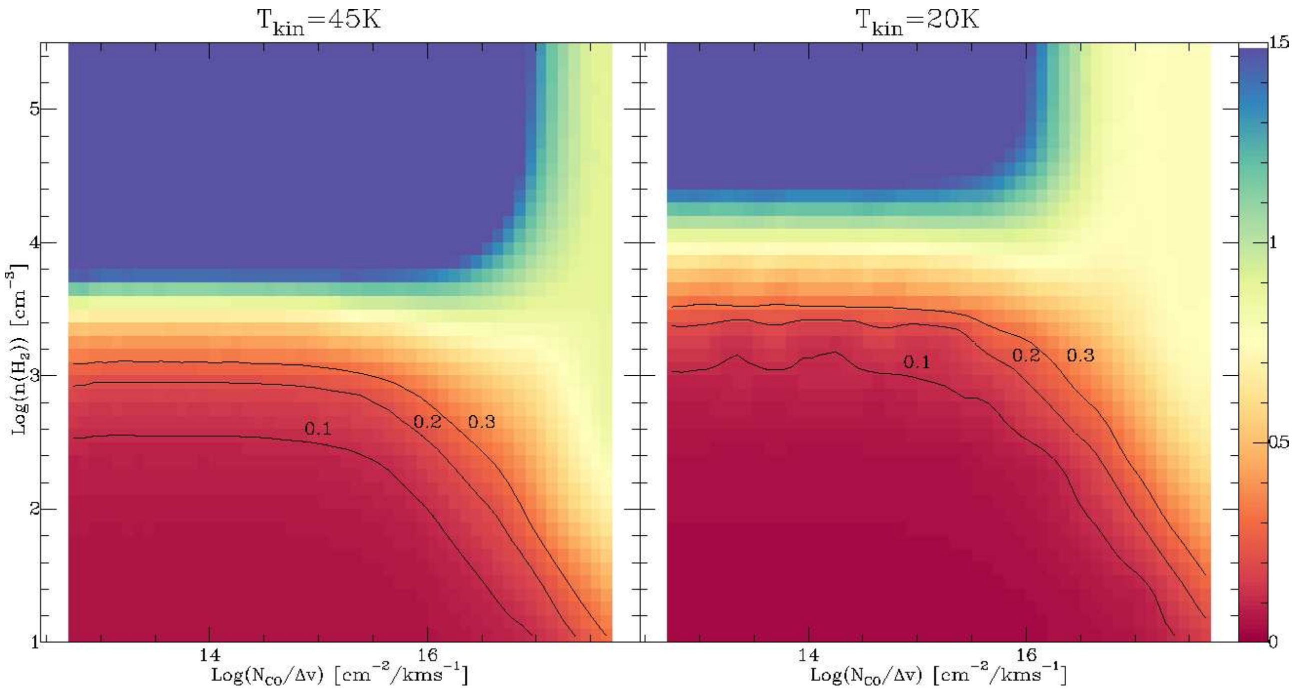

Fig. 5. Peak T_b ratio between the CO(3-2) and CO(1-0) lines versus the H_2 density, and the CO column density per unit velocity width ($N_{CO}/\Delta V$) for two values of the kinetic temperature: T_k = 45K, the dust temperature (left), andT_k = 20K (right). The black contours are underlining the values obtained in the data. The predictions come from the LVG hypothesis in the Radex code.

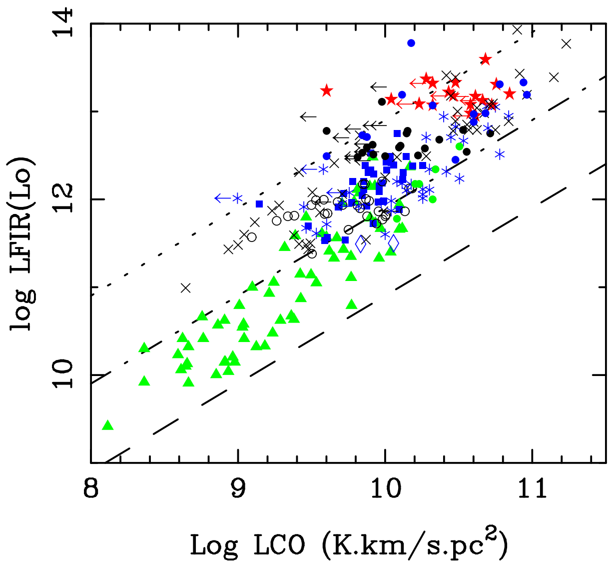

Fig. 7. Correlation between FIR and CO luminosities, for our sample (full black circles, and arrows for upper limits) and the other points from the literature (same symbols as in Fig 6). The 3 lines are for $L_{FIR}/M(H_2)$=10, 100 and 1000 $L_\odot/M_\odot$ from bottom to top, assuming a conversion factor α = 0.8 $M_\odot$ (K km s^{-1} pc^2)$^{-1}$. The three lines correspond to gas depletion time-scales of 580, 58 and 5.8 Myr respectively.

increase to up to 550 if the standard (MW) conversion factor is used. For local ULIRGs, this number is around 100 (Solomon et al. 1997), and 700 for normal galaxies (Wiklind et al. 1995), when calculated from IRAS fluxes.

We should note that the dust temperature has been measured from 60 and 100μm fluxes, which correspond to (1+z) higher frequencies in the rest frame of the galaxies. Therefore we are not sensitive to the very cold dust.

4.6. Activity of the galaxies

We have made a census of the different activities occuring in our sample galaxies. The last column of Table 4 indicates nuclear AGN activity, and perturbed morphology. These have been derived from the SDSS images, some of which are shown in Figure 8. We note that among the 12 non-detections, there are only 4 active objects, all being Seyfert 1 or quasars, while among the 18 detected ones, there are 12 active objects, and most of the time they are LINERs, Seyfert 2, and show signs of galaxy interactions and mergers.

4.7. Star formation efficiency

In the following we adopt the definition of SFE = $L_{FIR}/M(H_2)$, with a constant CO-to-H_2 conversion factor. The average SFE in our sample is 555 $L_\odot/M_\odot$, 3 times higher than that of the local ULIRGs (170 $L_\odot/M_\odot$). It should be kept in mind that some galaxies could have a different conversion factor, and this uncertainty affects our conclusions. Also, it is possible that the local SFR tracers evolve with time, and that, for a given SFR, different amounts of gas are consumed in star formation, if the IMF (Initial Mass Function) is different for earlier and younger galaxies. However, no strong evidence has been found until now for a significantly changing IMF, and the star formation laws are remarkably constant over redshift, as discussed by Genzel et al. (2010) and Daddi et al. (2010). We plot the SFE versus L'_{CO} in Figure 9, versus L_{FIR} in Figure 10, and versus the dust temperature in Figure 11.

What is obvious in all these figures is that galaxies of our sample are among the most efficient forming stars, and G19 and G27 even lie above the starbursts at high redshift. They are not

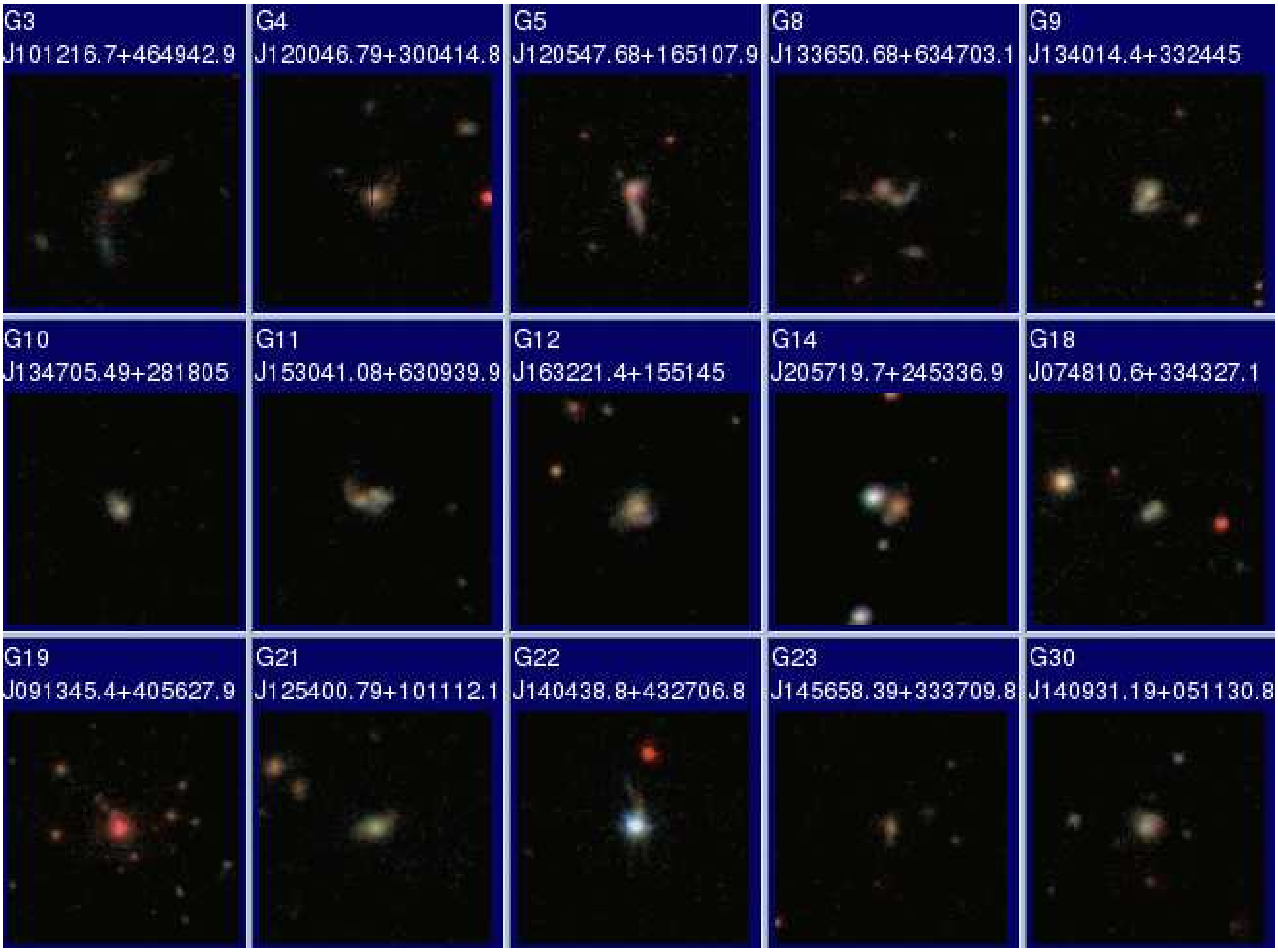

Fig. 8. Optical color images from the Sloan Digital Sky Survey (SDSS, http://www.sdss.org/) of 15 of our sources. They are all detections, except G10 and G21. Each panel is 50″x50″ in size, and is centered on the galaxy coordinates of Table 1.

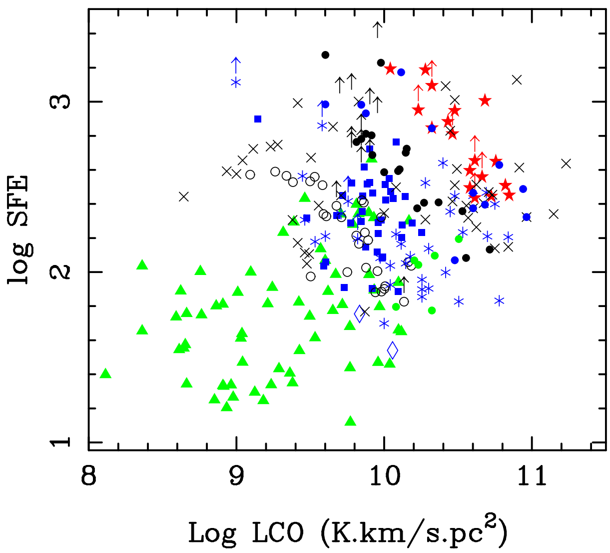

Fig. 9. Star formation efficiency SFE=$L_{FIR}/M(H_2)$, versus CO luminosity, assuming the same CO-to-H_2 conversion factor α = 0.8 $M_\odot$ (K km s^{-1} pc^2)$^{-1}$. All symbols are as defined in Fig 6.

among the most gas-rich, according to the CO luminosity. They could be experiencing a burst due to galaxy interactions. This is the case for G19 (Figure 8). No image is available for G27 (which lies outside of the footprint of the SDSS). Note that, as expected, there is a much larger correlation between SFE and L_{FIR}, than with L'_{CO}. The presence of large amounts of gas is not a sufficient condition to trigger a starburst, and another hidden factor is the extent of the spatial distribution of the molecular gas.

Finally, there is a correlation between the dust temperature and the SFE in Figure 11: it is conceivable that a concentrated starburst heats more efficiently the dust around it. However, the correlation becomes more scattered at higher redshifts, where the largest efficiencies occur. It is possible that our estimation of the dust temperature is not as accurate for these more redshifted objects. It is interesting to note the evolution of SFE with redshift, where our two most efficient starbursts are clearly noticeable (Figure 12). We compare this evolution with the cosmic star formation history, as compiled by Hopkins & Beacom (2006), from different works in the literature, and complemented at very high redshift by the gamma-ray burst (GRB) data by Kistler et al. (2009) and the optical data (Lyman-Break Galaxies, LBG) from Bouwens et al. (2008). The schematic curve in log reproduce the relative variations, whatever the vertical units, and can be arbitrarily translated vertically. Our points correspond to the most drastic change in this curve, and our following study at 0.6 < z < 1 should give more insight in this epoch.

Table 4. Molecular gas mass and star formation efficiency

G	$M(H_2)$ 10^9 $M_\odot$	SFE $L_\odot/M_\odot$	T_d K	M_d 10^8 $M_\odot$	Type
G1	28.6	120.	51.6	0.8	
G2	<7.5	>910.	47.0	2.6	
G3	5.8	667.	46.5	1.6	L, Int
G4	13.4	238.	46.7	1.2	L
G5	6.7	483.	48.1	1.1	L, Int
G6	<5.3	>521.	54.4	0.5	S1,Q
G7	<9.4	>928.	56.5	1.2	
G8	7.9	391.	44.5	1.6	Pair
G9	5.3	565.	48.7	0.9	S2, Int
G10	<4.6	>637.	47.4	1.0	
G11	14.9	255.	46.9	1.4	Int
G12	18.6	255.	46.0	2.0	L, Int
G13	<6.3	>1110.	43.8	4.0	S1,Q
G14	5.8	584.	45.7	1.5	
G15	27.0	227.	53.5	1.1	
G16	<5.3	>802.	42.7	2.9	
G17	57.1	67.	44.9	2.0	
G18	41.4	134.	43.5	3.4	
G19	3.2	1875.	>60.0	<0.5	Q2, Int
G20	<3.8	>1305.	44.6	2.8	
G21	<6.4	>542.	52.9	0.7	S2, Int
G22	6.6	626.	45.9	1.8	S1,Q, Int
G23	10.2	400.	42.1	3.3	
G24	<4.5	>1379.	36.6	11.9	S1,Q
G25	<4.9	>631.	38.5	4.0	
G26	<5.6	>615.	44.2	1.9	
G27	7.6	1699.	>49.0	<4.2	
G28	<7.3	>2615.	50.3	5.3	Q
G29	11.4	523.	54.5	1.0	Q
G30	11.2	497.	48.0	1.9	S2

L: LINER, S1, S2: Seyfert 1 & 2, Q: QSO, Int: interaction
$M(H_2)$ and SFE are defined in Sec. 4.2

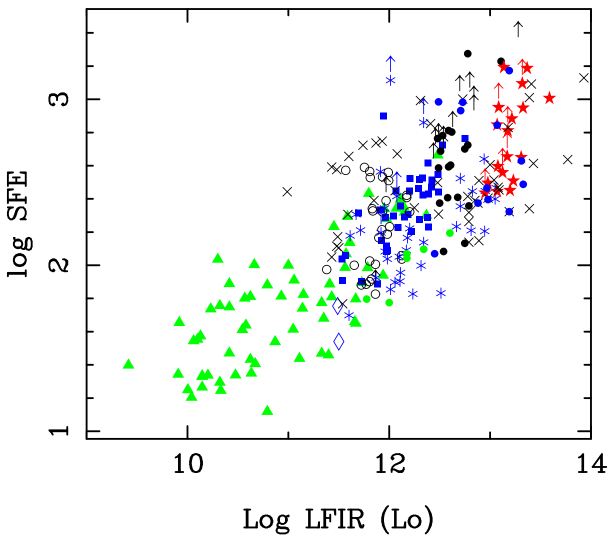

Fig. 10. Same as Figure 9, but versus L_{FIR}.

5. Discussion and conclusions

We have presented our search for CO-line emission in a sample of 30 ULIRGs, selected between 0.2 < z < 0.6 to fill the gap or "CO redshift desert" between z=0.1 and 1. We intend to cover the second part 0.6 < z < 1.0 in a following work. Our detection rate is ~ 60%. We find that some of the galaxies possess large amounts of molecular gas, much larger than local ULIRGs. Considering the evolution with cosmic time, it appears that the huge amounts of gas, common at high redshift, begin to disappear at z~ 0.3. This drop in gas content is reminiscent of the drop in the star formation history of the universe, which may imply that the change in star formation is due to a change in gas content. There are good reasons to think that galaxies are more gas rich at high redshift, and also that their gaseous medium is denser. The sizes of galaxies are predicted to vary as $(1+z)^{-1}$, and the implied higher gas pressure could increase the H_2/H I ratio. Following semi-analytical simulations, Obreschkow et al. (2009) followed the H_2/H I ratio statistically

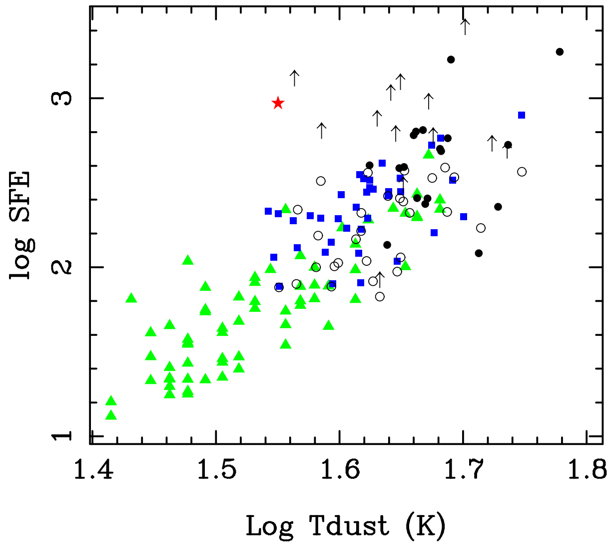

Fig. 11. Same as Figure 9, but versus T_d, for the sources where it could be defined. For the submillimeter galaxies, the red star corresponds to the averaged SFE, with the mean dust temperature of 35.5 found by Kovacs et al. (2010).

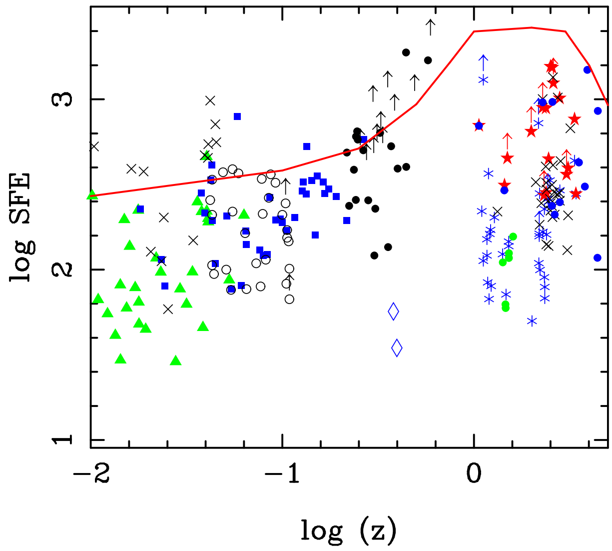

Fig. 12. Same as Figure 9, but versus redshift. The red curve is a schematic line summarizing the cosmic star formation history, from the compilation by Hopkins & Beacom (2006), complemented with the GRB data by Kistler et al. (2009) and the optical data from Bouwens et al. (2008) (the curve in log is only indicative of relative variations, independent of physical units, and can be translated vertically.)

over 30 million galaxies, and its cosmic decline has been modelled as $\Omega_{H_2}/\Omega_{HI} \propto (1+z)^{1.6}$ by Obreschkow & Rawlings (2009). This law appears to reproduce grossly the decline in the maximum L'_{CO} with time, as shown in Figure 6. Some galaxies of our sample, however, lie significantly above this envelope. The increase with z in the H_2 content of galaxies might occur already at lower z than this model predicts.

Five of our galaxies were observed in both CO(3-2) and CO(1-0) lines, allowing an estimation of the excitation temperature. They appear all very low, similar to what is observed in the Milky Way, or more normal galaxies, but also some local ULIRGs (Radford et al 1991). These ULIRGs could be similar to those discovered by Daddi et al. (2008) at redshift z∼1.5. If a galactic conversion factor was adopted for these galaxies, as suggested by Daddi et al (2010), their H_2 mass would be even higher, and they would stand out even more in the cosmic H_2 abundance.

It is also possible that the star formation decline between z=1 and z=0 is partly due to the declining star forming efficiency. For galaxies of our sample, the star formation efficiency (SFE) appears very high, in comparison to the most active starbursts at different redshifts. This supports a high contribution of the SFE to the star formation variations with redshift, although we are observing an increase of efficiency of the most extreme objects. It is possible to compare the observed time gradients in the cosmic star formation rate, and those in the extreme SFE in Figure 12. We observe a significant gradient in SFE, but however less steep than in the star formation history. The latter requires also a strong variation in gas content.

The very efficient star forming objects (ULIRGs) dominates the star formation at high redshift (z < 1.5, Lefloc'h et al. 2005), and less extreme objects (LIRGs) dominate later on (Caputi et al. 2006), which might explain the strong decline in efficiency between z=1 and 0. It appears that the range of redshift studied here is just where the most massive objects continue to form stars with unprecedented efficiency, before the sudden drop due to star formation quenching (e.g. Springel et al. 2005).

Acknowledgements. The authors gratefully acknowledge the IRAM staff for their help in the data acquisition. We have made use of the NASA/IPAC Extragalactic Database (NED).

References

Blain A.W., Longair M.S.: 1996, MNRAS 279, 847
Blain A.W., Smail I., Ivison R.J., Kneib J-P.: 1999, MNRAS 302, 632
Bouwens R.J., Illingworth G.D., Franx M., Ford H.: 2008, ApJ 686, 230
Brown R.L., Vanden Bout P.A.: 1991, AJ 102, 1956
Caputi K.I., Dole H., Lagache G. et al.: 2006, A&A 454, 143
Chung, A., Narayanan, G., Yun, M. S., Heyer, M.,Erickson, N.R.: 2009, AJ 138, 858
Clements, D., Sutherland, W. Saunders, W. et al.: 1996, MNRAS 279, 459 & 477
Combes F., Maoli R., Omont A.: 1999, A&A 345, 369
Combes, F., García-Burillo, S., Braine, J. et al.: 2006, A&A 460, L49 **(paper I)**
Daddi E., Dannerbauer H., Elbaz D. et al.: 2008 ApJ 673, L21
Daddi E., Bournaud, F., Walter, F.et al.: 2010 ApJ 713, 686
Downes D., Solomon P., Radford S.J.E.: 1993, ApJ 414, L13
Downes D., Solomon P.: 1998, ApJ 507, 615
Gao Y., Solomon P.M.: 2004 ApJS 152, 63
Geach, J.E., Smail I., Coppin K. et al.: 2009, MNRAS 395, L62
Genzel, R., Tacconi, L. J. et al.: 2010, MNRAS, in press, arXiv1003.5180
Greve. T.R., Bertoldi, F., Smail, I. et al.: 2005, MNRAS, 359, 1165
Hildebrand R. H., 1983, QJRAS, 24, 267
Hinshaw G., Weiland J.L., Hill R.S. et al.: 2009, ApJS 180, 225
Hopkins, A.M., Beacom J.F.: 2006, ApJ, 651, 142
Iono, D., Wilson, C. D., Yun, M.S. et al.: 2009, ApJ, 695, 1537
Kennicutt R.C.: 1998, ApJ 498, 541
Kim D.C., Sanders D.B.: 1998, ApJS 119, 41
Kim D.C., Veilleux S., Sanders D.B.: 1998, ApJ 508, 627
Kim D.C., Veilleux S., Sanders D.B.: 2002, ApJS 143, 277
Kovacs A., Omont A., Beelen A. et al.: 2010, ApJ 717, 29
Kistler M.D., Yüksel H., Beacom J.F. et al.: 2009, ApJ 705, L104
Le Fèvre O., Abraham R., Lilly S.J. et al.: 2002, MNRAS 311, 565
Lefloc'h E., Papovich C., Dole H. et al.: 2005, ApJ 632, 169
Lo K-Y., Chen H-W., Ho P.T.P.: 1999, A&A 341, 348
Madau P., Pozzetti L., Dickinson M.E.: 1998, ApJ 498, 106
Melchior A.-L., Combes F.: 2008, A&A 477, 775
Obreschkow, D., Croton, D., De Lucia, G. et al.: 2009, ApJ 698, 1467
Obreschkow, D., Rawlings, S.: 2009ApJ 696, L129
Omont A., Beelen A., Bertoldi F. et al.: 2003, A&A 398, 857
Radford S.J.E., Downes D., Solomon P.M.: 1991, ApJ 368, L15
Riechers, D.A., Walter, F., Bertoldi, F. et al.: 2009, ApJ 703, 1338
Sanders D.S., Mirabel F., 1996, ARAA, 34, 749
Solomon P., Radford S., Downes D.: 1992 Nature 356, 318
Solomon P., Downes D., Radford S., Barrett J.: 1997, ApJ 478, 144
Solomon P., Vanden Bout P.A.: 2005, ARAA 43, 677
Springel V., Di Matteo T., Hernquist L.: 2005, ApJ 620, L79
Stanford S.A., Stern D., van Breugel W., de Breuck C.: 2000 ApJS 131, 185
Tacconi L.J., Genzel R., Neri R. et al.: 2010, Nature 463, 781
van der Tak, F. F. S., Black, J. H., Schöier, F. L.. et al.: 2007, A&A 468, 627
Wang, R., Carilli, C. L., Neri, R. et al.: 2010, ApJ 714, 699
Weiss, A., Henkel, C., Downes, D., Walter, F.: 2003, A&A 409, L41
Weiss, A., Downes, D., Walter, F., Henkel, 2007, ASPC 375, 25
Wiklind T., Combes F., Henkel C.: 1995, A&A 297, 643
Wilson C.D., Combes F.: 1998, A&A 330, 63
Wink J.E, Guilloteau S., Wilson T.: 1997 A&A 322, 427
Young J.S., Scoville N.Z.: 1991, ARAA 29, 581